

Mott Transition and Anomalous Resistive State in the Pyrochlore Molybdates

Nyayabanta Swain and Pinaki Majumdar
 Harish-Chandra Research Institute,
 Chhatnag Road, Jhusi, Allahabad 211019, India
 (Dated: November 7, 2016)

The rare earth based pyrochlore molybdates involve orbitally degenerate electrons Hund's coupled to local moments. The large Hund's coupling promotes ferromagnetism, the superexchange between the local moments prefers antiferromagnetism, and Hubbard repulsion tries to open a Mott gap. The phase competition is tuned by the rare earth ionic radius, decreasing which leads to change from a ferromagnetic metal to a spin disordered highly resistive ground state, and ultimately an 'Anderson-Mott' insulator. We attempt a quantitative theory of the molybdates by studying their minimal model on a pyrochlore geometry, using a static auxiliary field based Monte Carlo. We establish a thermal phase diagram that closely corresponds to the experiments, predict the hitherto unexplored orbital correlations, quantify and explain the origin of the anomalous resistivity, and present dynamical properties across the metal-insulator transition.

Traditional Mott materials involve a strong on-site Coulomb interaction that, beyond a critical value, and at integer filling, inhibits electron motion [1]. This, in a clean material, leads to an abrupt change in the zero temperature state from perfectly conducting to non conducting. The non conducting state typically has strong antiferromagnetic (AF) correlations, if not long range order, since that lowers the kinetic energy.

The Mott transition on a frustrated structure brings in a novelty since the AF ordered state in the Mott phase cannot be realised and one may have the signatures of a 'spin liquid' [2, 3]. Such phases are realised in some triangular lattice organics [4–6]. The pyrochlores [7] are also highly frustrated structures, much studied for possible spin liquid phases, but the rare earth molybdates, $R_2Mo_2O_7$, add additional twists to the Mott problem: (i) the Mott transition in these materials occur in the background of overall *ferromagnetic* correlation [7–9], and (ii) the zero temperature resistivity seems to grow continuously with the control parameter [10] (see next) rather than have an abrupt zero to infinity transition. These features owe their origin to the additional degrees of freedom, and couplings, involved in these materials.

The $R_2Mo_2O_7$ family exhibit ground states that vary from a ferromagnetic metal (FM) to a spin glass metal (SG-M) and then a spin glass insulator (SG-I) as the rare earth radius r_R is reduced [11]. Materials with $R = Nd$ and Sm are metallic, $R = Tb, Dy, Ho, Er$, and Y are insulating, and $R=Gd$ is on the verge of the insulator-metal transition (IMT) [7, 9, 10]. The unusual features in transport include very large residual resistivity, $\sim 10 m\Omega cm$ close to the metal-insulator transition [10], prominent anomalous Hall effect in metallic samples, e.g., $Nd_2Mo_2O_7$ [13–17], and magnetic field driven metallisation in the weakly insulating samples, e.g., $Gd_2Mo_2O_7$ [18].

The qualitative physics behind these effects is not a mystery, but several major questions remain unanswered, e.g., on (i) the simultaneity of the metal-insulator and magnetic transition in the ground state, (ii) thermal scales for the magnetic transitions, (iii) the orbital state, whose fate is entangled with the spin state, and (iv) transport near the Mott transition.

We employ a real space approach, using a static auxiliary

orbital field to handle the Hubbard interaction, and solve the resulting 'electron - local moment - orbital moment' problem via a Monte Carlo scheme on the pyrochlore lattice. After making parameter choices suggested by *ab initio* estimates [6, 20] our main results are as follows.

(i) We obtain a phase diagram with ferromagnetic metal and spin disordered metal and insulator phases. However, our disordered state is a 'spin liquid' in contrast to the experimental spin glass. (ii) The FM T_c is in the experimental ballpark if we make room for a simple renormalisation of the Hund's coupling. (iii) Our transport results bears almost quantitative correspondence with experiments [7, 10], explain the high residual resistivity in terms of spin and orbital disorder scattering, and predict a highly non monotonic temperature dependence for samples of the form $Gd_{2-x}Sm_xMo_2O_7$. (iv) The temperature and correlation dependence of our intermediate frequency optical spectral weight is very similar to the experiments [7, 10] but changing the cutoff frequency reveals peculiarities, also reflected in the single particle weight.

The $R_2Mo_2O_7$ structure consists of two interpenetrating pyrochlore lattices, one formed by Mo cations and the other by R. The Mo atom has octahedral oxygen coordination. The resulting crystal field splits the fivefold degenerate Mo 4d states into doubly degenerate e_g and triply degenerate t_{2g} manifolds, and a trigonal distortion splits the t_{2g} further into a nondegenerate a_{1g} and a doubly degenerate e'_g [6]. The Mo cation is nominally tetravalent and has two electrons on average. The deeper a_{1g} electron behaves like a local moment, and the single electron in the two e'_g orbitals is the 'itinerant' degree of freedom [6]. The e_g state remains unoccupied. In the limit of strong Hund's coupling between the a_{1g} and e'_g electrons we have (see Supplement):

$$H = \sum_{\langle ij \rangle, \alpha\beta} \tilde{t}_{ij}^{\alpha\beta} \tilde{c}_{i\alpha}^\dagger \tilde{c}_{j\beta} + J_{AF} \sum_{\langle ij \rangle} \mathbf{S}_i \cdot \mathbf{S}_j + U \sum_i n_{i\alpha} n_{i\beta}^{\alpha \neq \beta}$$

The first term is the kinetic energy of 'spinless' fermions, involving nearest neighbour intra and inter-orbital e'_g hopping. The ij dependence is determined by orientation of the a_{1g} moments on nearest neighbour sites. If $\mathbf{S}_i =$

$(\sin\theta_i\cos\phi_i, \sin\theta_i\sin\phi_i, \cos\theta_i)$ then $t_{ij}^{\alpha\beta} = [\cos\frac{\theta_i}{2}\cos\frac{\theta_j}{2} + \sin\frac{\theta_i}{2}\sin\frac{\theta_j}{2}e^{-i(\phi_i-\phi_j)}]t^{\alpha\beta}$, with $t^{11} = t^{22} = t$ and $t^{12} = t^{21} = t'$. We set $t' = 1.5t$ as suggested by density functional theory [20]. J_{AF} is the AF superexchange coupling between local moments at neighbouring sites on the pyrochlore lattice. $U > 0$ is the inter-orbital Hubbard repulsion.

The first two terms represent fermions in a classical spin background and the resulting magnetic phase competition has been studied on a pyrochlore lattice [21]. While these results are interesting they miss out on the large correlation scale, U , that drives the Mott transition. One option is to treat the model within dynamical mean field theory (DMFT) [22], but then the spatial character crucial to the pyrochlore lattice is lost.

We opt to handle the problem in real space as follows: (i) We use a Hubbard-Stratonovich (HS) [2–4] transformation that decouples $Un_{i\alpha}n_{i\beta}$ in terms of an auxiliary orbital moment $\Gamma_i(\tau)$, coupling to $\mathbf{O}_i = \sum_{\mu\nu} c_{i\mu}^\dagger \vec{\sigma}_{\mu\nu} c_{i\nu}$, and a scalar field $\Phi_i(\tau)$ coupling to n_i at each site (see Supplement). (ii) An exact treatment of the resulting functional integral requires quantum Monte Carlo. We retain only the zero Matsubara frequency modes of Γ_i and Φ_i , *i.e.*, approximate them as classical fields. (iii) The spatial thermal fluctuations of Γ_i are completely retained, while Φ_i is treated at the saddle point level, setting $\Phi_i \rightarrow \langle \Phi_i \rangle = (U/2)\langle n_i \rangle = U/2$ at half-filling (since charge fluctuations are expensive at large U). This method overall is known as a ‘static path approximation’ (SPA) to the functional integral for the many body partition function and has been used earlier in several problems [26–28]. This leads to a more tractable problem.

$$H_{eff} = \sum_{\langle ij \rangle} t_{ij}^{\alpha\beta} \tilde{c}_{i\alpha}^\dagger \tilde{c}_{j\beta} - \frac{U}{2} \sum_i \Gamma_i \cdot \mathbf{O}_i + J_{AF} \sum_{\langle ij \rangle} \mathbf{S}_i \cdot \mathbf{S}_j + H_{cl}$$

$H_{cl} = \frac{U}{4} \sum_i \Gamma_i^2$ and we have not explicitly written the term $(\mu - \frac{U}{2}) \sum_i n_i$, μ being the chemical potential. The localized spin and orbital moment configurations follow the distribution

$$P\{\mathbf{S}_i, \Gamma_i\} \propto \text{Tr}_{cc^\dagger} e^{-\beta H_{eff}}$$

Within the SPA scheme H_{eff} and $P\{\mathbf{S}_i, \Gamma_i\}$ define a coupled ‘fermion - local moment - orbital moment’ problem.

There are regimes where some analytic progress can be made, but our results here are based on a Monte Carlo solution of the model above - generating the equilibrium configurations of $\{\mathbf{S}_i, \Gamma_i\}$ through iterative diagonalisation of H_{eff} . To access large sizes within reasonable time we use a cluster algorithm [29, 30] for estimating the update cost (see Supplement). Results in this paper are for a $6 \times 6 \times 6$ pyrochlore lattice of ~ 800 sites.

From the equilibrium configurations we calculate the thermally averaged magnetic structure factor $S_{mag}(\mathbf{q}) = \frac{1}{N^2} \sum_{ij} \langle \mathbf{S}_i \cdot \mathbf{S}_j \rangle e^{i\mathbf{q} \cdot (\mathbf{r}_i - \mathbf{r}_j)}$ and orbital structure factor $S_{orb}(\mathbf{q}) = \frac{1}{N^2} \sum_{ij} \langle \Gamma_i \cdot \Gamma_j \rangle e^{i\mathbf{q} \cdot (\mathbf{r}_i - \mathbf{r}_j)}$ at each temperature. Electronic properties are calculated by diagonalising H_{eff} on equilibrium backgrounds.

We will discuss the physics of the model for a wide range of $J_{AF} - U - T$ in a separate paper and focus here on parameters appropriate to the molybdates. Following *ab initio* estimates [6, 20] we use $t = 0.1$ eV and $J_{AF} = 0.02$ eV. The calibration of U/t in terms of r_R is based on the optical gap (see Supplement). For the molybdates U/t seems to vary from $\sim 5 - 9$ as R varies from Nd to Ho. We discuss results for the chosen t , J_{AF} , and U/t , using absolute scales, and compare with available experimental data [10, 31].

Phase diagram: Fig.1.(a) shows the experimental phase diagram. At large r_R , where the U/t ratio is relatively small, the ground state is a ferromagnetic metal with a moment $\sim 1.4\mu_B$ per Mo [14, 31]. The magnetisation seems to diminish slowly as r_R reduces (panel 1.(c)), and then rapidly around the metal-insulator transition, $r_R^c \sim 1.06\text{\AA}$, but a small value survives into the weak insulating regime [31]. The FM T_c is $\sim 80\text{K}$ for large r_R and drops sharply near r_R^c . The state for $r_R \lesssim r_R^c$ is a spin glass, with $T_{SG} \sim 20\text{K}$.

Panel 1.(b) shows our result over the window $U/t \sim 5 - 10$. For our parameter calibration the metal-insulator transition (MIT) at $T = 0$ occurs at $U_c \sim 7.6t$, and we present our results in terms of U_c/U . At the right end, where $U \sim 0.7U_c$, the ground state is metallic, double exchange (DE) dominated, and an almost saturated ferromagnet. This is also a weakly ‘ferro orbital’ state. With increasing U the orbital moment

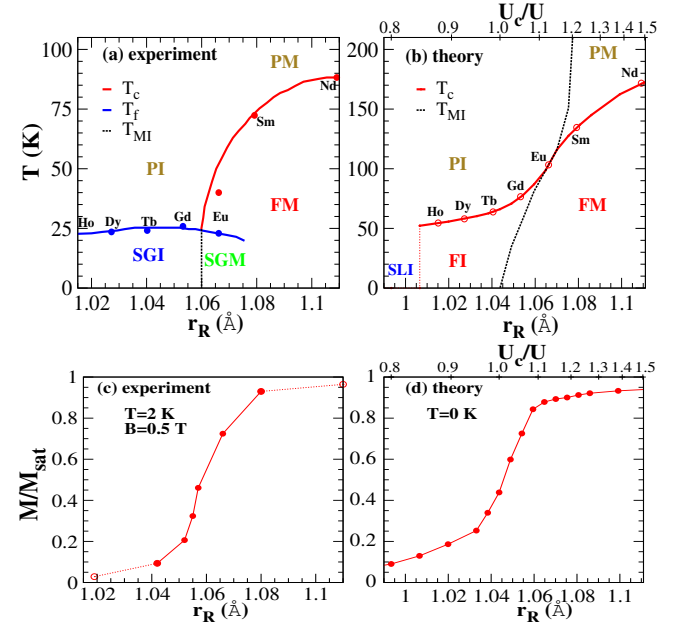


FIG. 1. Colour online: (a)-(b) Phase diagram of the molybdates- experiment [11, 13] and theory. The experimental ground state changes from ferromagnetic metal (FM) to spin-glass metal (SGM) and then spin-glass insulator (SGI) with reducing r_R . Within theory the FM transforms to a ‘spin liquid’ rather than a spin-glass. (c)-(d) Show the ferromagnetic moment at low T as the system is taken through the MIT. Within both experiment [31], (c), and theory, (d), a small moment survives in the insulator. In (b) we have cut off T_c at the point where the $T = 0$ magnetisation drops below 10%.

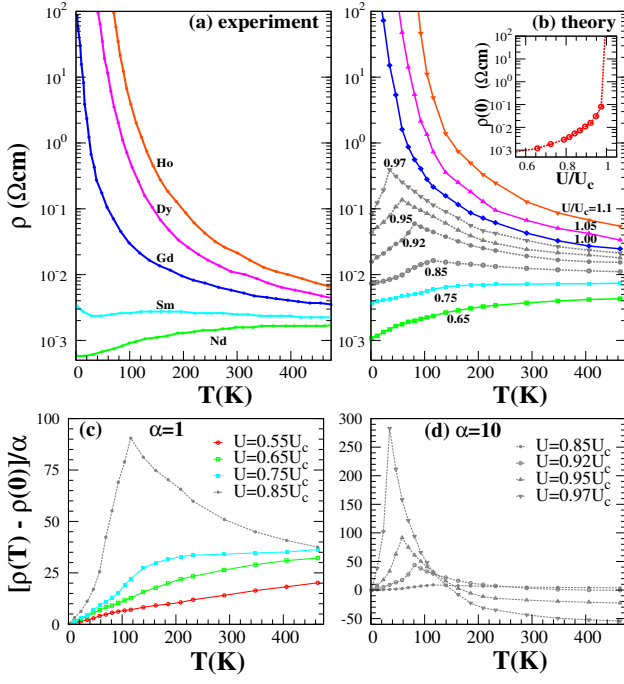


FIG. 2. Colour online: (a) Resistivity of the molybdates for varying rare earth [10]. (b) Resistivity computed within our scheme. The coloured plots are counterparts of the experimental data, while the dotted lines predict possible behaviour if intermediate compositions were to be synthesized. Inset to (b) shows the growth of the ‘residual’ resistivity, $\rho(0)$. (c)-(d) Show theory results for $\rho(T) - \rho(0)$ on a linear scale, to highlight the temperature driven metal to insulator crossover.

grows and leads to a splitting of the e'_g band.

What drives the metal-insulator transition? (i) Increasing U increases the splitting $\Delta \sim |T|U$ between the electronic levels on Mo. This becoming comparable to the bandwidth would lead to a Mott transition (the correlation aspect). (ii) With increasing U , the growing orbital moment suppresses the electron kinetic energy. This weakens DE. The competing AF superexchange reduces the magnetisation and increases the extent of spin disorder in the ground state. We call this the ‘Anderson’ (disorder) aspect of the problem. It depends crucially on the presence of J_{AF} . U_c is determined by a combination of the Mott and Anderson effects opening a gap in the electronic spectrum. Since magnetic disorder plays a role in the MIT, one can affect the transition by applying a magnetic field [18].

Temperature scales: We have used a model with Hund’s coupling $J_H \gg t$ for convenience, and obtain $T_c \sim 160\text{K}$ for Nd. In reality $J_H \sim 5t$ [6], and as earlier results show [8] this would reduce T_c by $\sim 50\%$ to about 80K (see Supplement), close to the actual value for Nd. Within our scheme we do not find any spin freezing, so no T_{SG} . Our magnetic state for $U \gtrsim U_c$ is a spin liquid (SL), rather than a spin glass, with weak ferromagnetism. We comment on the spin freezing issue later. Panels 1.(c) and 1.(d) show the low T magnetisation in the molybdates and in our scheme. The dependence is very similar and a small magnetization survives beyond the MIT.

Resistivity: We demarcate the finite T metal-insulator boundary based on the temperature derivative of resistivity $d\rho/dT$: ‘metal’ if $d\rho/dT > 0$, ‘insulator’ if $d\rho/dT < 0$. We compute $\rho(T)$ via the low-energy limit of the optical conductivity [5] (see Supplement). Fig.2.(a) shows experimental resistivity [10] while 2.(b) shows the theory result for parameter values set by the calibration.

Even the limited R variation in the experiments can be thought to represent three ‘regimes’. (i) For $R=\text{Nd}$, the ‘high T_c ’ FM, $\rho(T)$ has traditional metallic behaviour, $\rho(0) < 1 \text{ m}\Omega\text{cm}$ and $d\rho/dT > 0$ all the way to 400K. (ii) For $R=\text{Gd, Dy, Ho}$, the system is insulating at all T , with $\rho(0) \rightarrow \infty$. The behaviour is clearly activated for Dy and Ho while Gd seems to be weakly insulating. (iii) $R=\text{Sm}$ (and Eu, not shown) represents the most interesting case, with $\rho(0) \sim 3 \text{ m}\Omega\text{cm}$ and a non monotonic T dependence [7, 10]. Any theory would have to capture the obvious regimes (i) and (ii) and also the peculiar large $\rho(0)$ and non monotonicity in (iii).

Our results, panel 2.(b), show the following: (i) For $U \ll U_c$, the itinerant e'_g electrons see a DE dominated ferromagnetic background, as well as an orbital-ferro state. The $T = 0$ state is ideally clean, and finite T resistivity from spin and orbital fluctuations generate an approximate linear T behaviour (see 2.(c)). (ii) For $U \gg U_c$, there is a distinct gap Δ with $\rho(T) \sim \rho_0 e^{\Delta/T}$ as $T \rightarrow 0$ and $d\rho/dT < 0$ over the entire temperature range. (iii) For $U \lesssim U_c$, the residual resistivity $\rho(0)$ is finite. This arises from a combination of depleting DOS at the Fermi level (due to the increasing orbital moment), and the magnetic disorder due to weakening DE. The behaviour of $\rho(0)$ is shown in the inset to panel 2.(b). Increasing

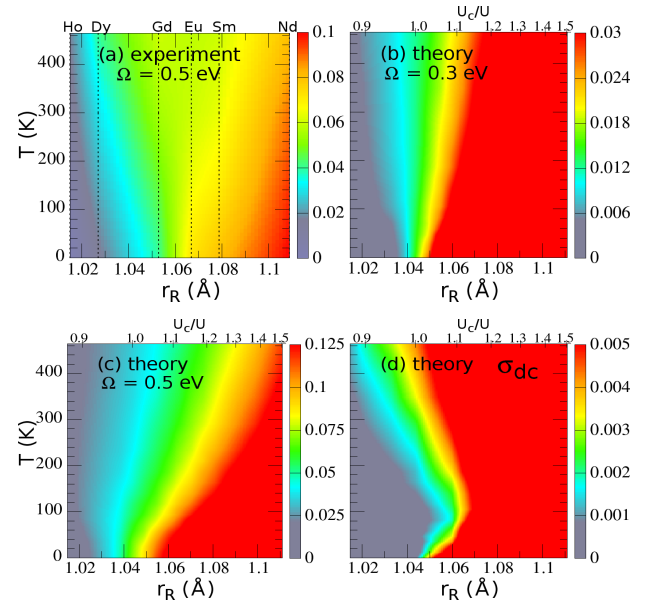


FIG. 3. Colour online: (a)-(c) Low energy optical spectral weight, $n_{eff} \propto \int_0^\Omega \sigma(\omega) d\omega$. (a) Experimental result for $\Omega = 0.5 \text{ eV}$ [10], (b) theory result for $\Omega = 0.3 \text{ eV}$, (c) theory result for $\Omega = 0.5 \text{ eV}$. (d) The d.c. conductivity within theory.

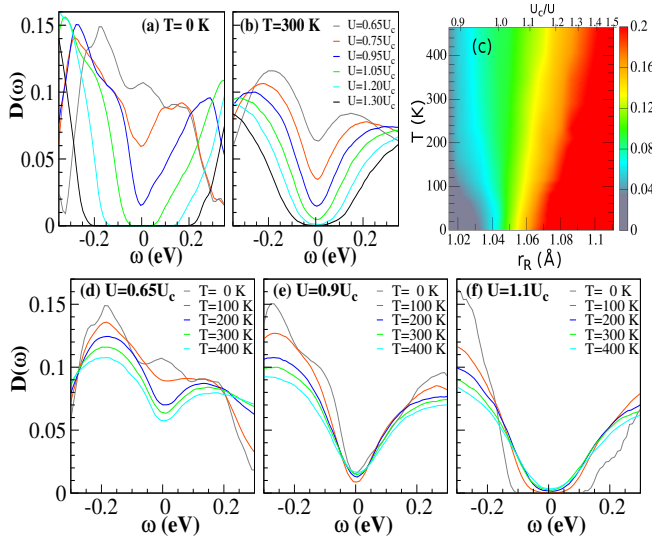


FIG. 4. Colour online: (a)-(b) Variation of density of states with U at $T = 0\text{K}$ and 300K . (c) Integrated DOS, over $\omega = \pm 0.15\text{eV}$, for varying U and T . (d)-(f) Temperature dependence of DOS at $U = 0.65U_c$, $0.9U_c$ and $1.1U_c$, respectively. (d) is a gapless metal, (e) shows a pseudogapped state, while (f) shows the T dependence in a gapped Mott insulator.

ing T does lead to a linear behaviour, with a large slope, but the resistivity peaks at a scale $T_{peak}(U)$ and falls thereafter. Panels 2.(c)-(d) highlight this trend. As $U \rightarrow U_c$, $T_{peak} \rightarrow 0$, finally merging with the insulating behaviour in (ii).

Optical spectral weight: Fig.3.(a) shows the experimentally estimated optical spectral weight $n_{eff}(\Omega) = (2m_0/\pi e^2) \int_0^\Omega \sigma(\omega) d\omega$ for different R and varying temperature at $\Omega = 0.5\text{ eV}$ [10]. It shows the expected trend of n_{eff} growing with T in the insulating, low r_R , side as the Mott gap is slowly filled, and reducing on the metallic side as weight gets transferred to high energy as coherence is lost.

We calculated the same quantity for different cutoff frequencies, Ω , as $n_{eff}(\Omega) = \int_0^\Omega \sigma(\omega) d\omega$. Fig.3.(b)-(c) show our result for $\Omega = 0.3\text{ eV}$ and 0.5 eV respectively. Panel 3.(d) shows just σ_{dc} to contrast the features in optical weight to the non monotonicity of the d.c conductivity itself.

Our result at $\Omega = 0.3\text{ eV}$, roughly $2/3$ the experimental cutoff, has the same features as the experimental data. At $\Omega = 0.5\text{ eV}$, however, our data reveal a weak non monotonicity in the T dependence when $U \gtrsim U_c$. This arises because $\sigma(\omega)$ gains weight at low frequency, as in panel (b), but *loses more* around $\omega \sim 0.5\text{ eV}$. The success in capturing the d.c resistivity, Fig.2, does not translate to similar success in the capturing the high energy optical conductivity. It is possible that some of the simplifying assumptions regarding bandstructure and coupling constants, *i.e* J_H , affect this result.

The non monotonicity in our $\Omega = 0.5\text{ eV}$ spectral weight (Fig.3.(c)) is distinct from the d.c conductivity behaviour shown in Fig.3.(d). Fig.2.(b) shows that bad $T = 0$ metals, for $U \lesssim U_c$, become more resistive with increasing T and beyond a T_{peak} become less resistive again. We suggest that a de-

tailed conductivity map, on materials like $\text{Gd}_{2-x}\text{Sm}_x\text{Mo}_2\text{O}_7$ or $\text{Gd}_{2-x}\text{Eu}_x\text{Mo}_2\text{O}_7$ could reveal this non monotonicity.

Density of states: We computed the single particle density of states (DOS), $D(\omega)$, for the interaction and temperature window studied. Fig.4.(a) shows the dependence of $D(\omega)$ on U/U_c as the system is driven across the Mott transition at $T = 0$. The DOS has its tight binding form upto $U \sim 0.7U_c$ beyond which the presence of the orbital moment shows a visible depletion in the DOS around $\omega = 0$. This dip becomes a gap for $U \geq U_c$, which grows in the insulating phase. At $T = 300\text{K}$, Fig.4.(b), the systems with $U < U_c$ *lose weight* near $\omega = 0$, while those with $U > U_c$ gain weight. Panel 4.(c) quantifies these trends by calculating $\int_{-\Omega'}^{\Omega'} N(\omega) d\omega$, where $\Omega' = 0.15\text{ eV}$ (to make a comparison with Fig.3.(b)). We suggest that the optical behaviour observed experimentally has an analog in the single particle spectral weight transfer as well.

Panels 4.(d)-(f) show the thermal evolution of the DOS at three representative U/U_c . (i) In 4.(d) $U \sim 0.6U_c$, the ground state is a nearly saturated ferromagnet with a small orbital moments Γ_i 's and has finite DOS at $\omega = 0$. Thermal growth and fluctuations of the Γ_i 's decrease the DOS at $\omega = 0$ resulting in a small dip at high temperature. (ii) For $U = 1.1U_c$, panel 4.(f), there is significant spin disorder in the ground state (the ferromagnetic moment is ~ 0.1) and the Γ_i 's are large, ~ 1 , at all sites. A remnant of the atomic gap $\sim U|\Gamma|$, survives despite the presence of hopping. The DOS shows a Mott gap. With increase in temperature, the angular fluctuations of the Γ_i 's result in a slight smearing of the gap edge and increase in 'low energy' weight. (iii) For $U = 0.9U_c$, panel 4.(e), the magnetic state has magnetisation, $M \sim 0.5$ and the Γ_i 's are moderately large. As a result there is only a loss in weight around $\omega = 0$ but no hard gap. This is a pseudogap state.

There are several molybdate effects that we have not touched upon in this short paper, but they can also be readily explored. These include (i) the experimental $P - r_R$ phase diagram, (ii) the field driven IMT in $\text{Gd}_2\text{Mo}_2\text{O}_7$ [18], (iii) anomalous Hall effect (AHE) observed in $\text{Nd}_2\text{Mo}_2\text{O}_7$ [13–17], and (iv) spin glass freezing, which requires some degree of quenched disorder [34] (or bond distortions [35–38]).

Conclusion: We provide the first study of the Mott transition in the pyrochlore molybdates, in a real space framework, retaining the double exchange, superexchange and correlation effects. Our phase diagram captures the transition from a ferromagnetic metal to a spin disordered insulator, as in experiments, with reasonable thermal scales. Our transport and optical results capture major features of the molybdate data, reveal unexplored non monotonicities, and, we predict, correlate with the single particle spectral weight. Ongoing work will address the field driven Anderson-Mott transition.

We acknowledge use of the HPC clusters at HRI.

- [2] P. W. Anderson, *Mater. Res. Bull.* **8**, 153 (1973).
- [3] L. Balents, *Nature* **464**, 199 (2010).
- [4] Y. Shimizu, K. Miyagawa, K. Kanoda, M. Maesato and G. Saito, *Phys. Rev. Lett.* **91**, 107001 (2003).
- [5] M. Yamashita, *et al.* *Nature Phys.* **5**, 44 (2009).
- [6] K. Kanoda and R. Kato, *Annu. Rev. Condens. Matter Phys.* **2**, 167 (2011).
- [7] J. S. Gardner, M. J. P. Gingras, and J. E. Greedan, *Rev. Mod. Phys.* **82**, 53 (2010).
- [8] J. E. Greedan, *et al.*, *J. Solid State Chem.* **68**, 300 (1987).
- [9] K. Miyoshi, *et al.*, *J. Magn. Magn. Mater.* **226**, 898 (2001).
- [10] I. Kezsmarki, *et al.*, *Phys. Rev. Lett.* **93**, 266401 (2004).
- [11] S. Iguchi, *et al.*, *Phys. Rev. Lett.* **102**, 136407 (2009).
- [12] I. Kezsmarki, *et al.*, *Phys. Rev. B* **73**, 125122 (2006).
- [13] T. Katsufuji, H.Y. Hwang and S.W. Cheong, *Phys. Rev. Lett.* **84**, 1998 (2000).
- [14] Y. Taguchi, *et al.*, *Science* **291**, 2573 (2001).
- [15] Y. Taguchi, *et al.*, *Phys. Rev. Lett.* **90**, 257202 (2003).
- [16] S. Iguchi, N. Hanasaki, and Y. Tokura, *Phys. Rev. Lett.* **99**, 077202 (2007).
- [17] K. Ueda, *et al.*, *Phys. Rev. Lett.* **108**, 156601 (2012).
- [18] N. Hanasaki, *et al.*, *Phys. Rev. Lett.* **96**, 116403 (2006).
- [19] I. V. Solovyev, *Phys. Rev. B* **67**, 174406 (2003).
- [20] H. Shinaoka, Y. Motome, T. Miyake, and S. Ishibashi, *Phys. Rev. B* **88**, 174422 (2013).
- [21] Y. Motome and N. Furukawa, *Phys. Rev. Lett.* **104**, 106407 (2010), *Phys. Rev. B* **82**, 060407(R) (2010).
- [22] A. Georges, *et al.*, *Rev. Mod. Phys.* **68**, 13 (1996).
- [23] R. L. Stratonovich, *Sov. Phys. Doklady* **2**, 416 (1958), J. Hubbard, *Phys. Rev. Lett.* **3**, 77 (1959).
- [24] J. Hubbard, *Phys. Rev. B* **19**, 2626 (1979).
- [25] H. J. Schulz, *Phys. Rev. Lett.* **65**, 2462 (1990).
- [26] M. Mayr, G. Alvarez, C. Sen, and E. Dagotto, *Phys. Rev. Lett.* **94**, 217001 (2005).
- [27] Y. Dubi, *et al.*, *Nature*, **449**, 876 (2007).
- [28] R. Tiwari and P. Majumdar, *Europhys. Lett.* **108**, 27007 (2014).
- [29] S. Kumar and P. Majumdar, *Eur. Phys. J. B*, **50**, 571 (2006).
- [30] A. Mukherjee, N.D. Patel, C. Bishop, and E. Dagotto, *Phys. Rev. E* **91**, 063303 (2015).
- [31] N. Hanasaki, *et al.*, *Phys. Rev. Lett.* **99**, 086401 (2007).
- [32] K. Pradhan and P. Majumdar, *Europhys. Lett.* **85**, 37007 (2009).
- [33] P. B. Allen in *Conceptual Foundation of Materials V.2*, edited by Steven G. Louie, Marvin L. Cohen, Elsevier (2006).
- [34] T. E. Saunders and J. T. Chalker, *Phys. Rev. Lett.* **98**, 157201 (2007).
- [35] A. Keren and J. S. Gardner, *Phys. Rev. Lett.* **87**, 177201 (2001).
- [36] E. Sagi, O. Ofer, A. Keren, and J.S. Gardner, *Phys. Rev. Lett.* **94**, 237202 (2005).
- [37] J. E. Greedan, *et al.*, *Phys. Rev. B* **79**, 014427 (2009).
- [38] H. Shinaoka, Y. Tomita, and Y. Motome, *Phys. Rev. Lett.* **107**, 047204 (2011), *Phys. Rev. B* **90**, 165119 (2014).

SUPPLEMENTARY INFORMATION: MOTT TRANSITION IN MOLYBDATES

Static path approximation (SPA) derivation of the effective Hamiltonian

The accepted model for the molybdate relevant degrees of freedom takes the following form [1]:

$$H = \sum_{\langle ij \rangle, \alpha\beta, \sigma} t_{ij}^{\alpha\beta} c_{i\alpha\sigma}^\dagger c_{j\beta\sigma} - J_H \sum_{i, \alpha} \mathbf{S}_i \cdot c_{i\alpha\sigma}^\dagger \vec{\sigma}_{\sigma\sigma'} c_{i\alpha\sigma'} + J_{AF} \sum_{\langle ij \rangle} \mathbf{S}_i \cdot \mathbf{S}_j + \sum_{i, \alpha\beta\alpha'\beta'}^{\sigma, \sigma'} U_{\alpha\beta}^{\alpha'\beta'} c_{i\alpha\sigma}^\dagger c_{i\beta\sigma'}^\dagger c_{i\beta'\sigma'} c_{i\alpha'\sigma}$$

The first term is the kinetic energy, involving nearest neighbour intra and inter-orbital e'_g hopping. The second term is the Hund's coupling between the a_{1g} local moment \mathbf{S}_i and the e'_g electrons, J_{AF} is the AF superexchange coupling between local moments at neighbouring sites on the pyrochlore lattice, and the U represents onsite e'_g Coulomb matrix elements.

To simplify the computational problem we treat the localized spins \mathbf{S}_i as classical unit vectors, absorbing the size S in the magnetic couplings. Also, to reduce the size of the Hilbert space we assume that $J_H/t \gg 1$, where t is the typical hopping scale, so that only the locally 'spin aligned' fermion state is retained. In this local basis the hopping matrix elements are dictated by the orientation of the \mathbf{S}_i on neighbouring sites.

Thus leads to a two orbital spinless Hubbard model.

$$H = \sum_{\langle ij \rangle, \alpha\beta} \tilde{t}_{ij}^{\alpha\beta} c_{i\alpha}^\dagger \tilde{c}_{j\beta} - \mu \sum_i n_i + U \sum_{i, \alpha \neq \beta} n_{i\alpha} n_{i\beta}$$

The partition function for the Hubbard model can be written as a functional integral over Grassmann fields $\psi_{i\alpha}(\tau)$ and $\bar{\psi}_{i\alpha}(\tau)$ as

$$Z = \int \mathcal{D}\psi \mathcal{D}\bar{\psi} e^{-\int_0^\beta d\tau \mathcal{L}(\tau)}$$

$$\mathcal{L}(\tau) = \sum_{\langle ij \rangle, \alpha\beta} \{ \bar{\psi}_{i\alpha} ((\partial_\tau - \mu) \delta_{ij} \delta_{\alpha\beta} + \tilde{t}_{ij}^{\alpha\beta}) \psi_{j\beta} \} + U \sum_{i, \alpha \neq \beta} \bar{\psi}_{i\alpha} \psi_{i\alpha} \bar{\psi}_{i\beta} \psi_{i\beta}$$

The quartic term is 'decoupled' exactly via a Hubbard-Stratonovich transformation [2-4]

$$e^{U \bar{\psi}_{i\alpha} \psi_{i\alpha} \bar{\psi}_{i\beta} \psi_{i\beta}} = \int \frac{d\Phi_i d\mathbf{\Gamma}_i}{4\pi^2 U} e^{(i\Phi_i n_i - \mathbf{\Gamma}_i \cdot \mathbf{O}_i + \frac{\Phi_i^2}{U} + \frac{\mathbf{\Gamma}_i^2}{U})}$$

where $\Phi_i(\tau)$ and $\mathbf{\Gamma}_i(\tau)$ are two auxiliary fields: $\Phi_i(\tau)$ coupling to charge density $n_i = n_{i\alpha} + n_{i\beta}$, and $\mathbf{\Gamma}_i(\tau)$ coupling to the orbital variable $\mathbf{O}_i = \sum_{\mu\nu} \bar{\psi}_{i\mu} \vec{\sigma}_{\mu\nu} \psi_{i\nu}$. This leads to the partition function,

$$Z = \int \mathcal{D}\psi \mathcal{D}\bar{\psi} \prod_i \frac{d\Phi_i d\mathbf{\Gamma}_i}{4\pi^2 U} e^{-\int_0^\beta d\tau \mathcal{L}(\tau)}$$

$$\mathcal{L}(\tau) = \mathcal{L}_0(\tau) + \mathcal{L}_{int}(\tau) + \mathcal{L}_{cl}(\tau)$$

$$\mathcal{L}_0(\tau) = \sum_{\langle ij \rangle, \alpha\beta} \{ \bar{\psi}_{i\alpha} ((\partial_\tau - \mu) \delta_{ij} \delta_{\alpha\beta} + \tilde{t}_{ij}^{\alpha\beta}) \psi_{j\beta} \}$$

$$\mathcal{L}_{int}(\tau) = \sum_i \{ i \Phi_i \bar{\psi}_{i\alpha} \psi_{i\alpha} - \mathbf{\Gamma}_i \cdot \bar{\psi}_{i\alpha} \vec{\sigma}_i \psi_{i\beta} \}$$

$$\mathcal{L}_{cl}(\tau) = \sum_i \left\{ \frac{\Phi_i^2}{U} + \frac{\mathbf{\Gamma}_i^2}{U} \right\}$$

To make further progress, we use the following two approximations: (i) neglect the imaginary time dependence of Φ_i and $\mathbf{\Gamma}_i$, i.e, retain only the zero Matsubara frequency modes of these fields, and (ii) replace Φ_i by its saddle point value $\langle \Phi_i \rangle = (U/2) \langle n_i \rangle = U/2$, since the important low energy fluctuations arise from the $\mathbf{\Gamma}_i$. Following this one can obtain the effective 'Hamiltonian' for the $\mathbf{\Gamma}_i$ by formally integrating out the $\psi, \bar{\psi}$:

$$H_{eff}\{\mathbf{\Gamma}_i\} = -\frac{1}{\beta} \log \text{Tr} e^{-\beta H_{el}} + \frac{1}{U} \sum_i \mathbf{\Gamma}_i^2$$

$$H_{el} = \sum_{ij}^{\alpha\beta} \tilde{t}_{ij}^{\alpha\beta} c_{i\alpha}^\dagger c_{j\beta} - \tilde{\mu} \sum_i n_i - \sum_i \mathbf{\Gamma}_i \cdot \mathbf{O}_i$$

and $\tilde{\mu} = \mu - U/2$. For convenience we redefine $\mathbf{\Gamma}_i \rightarrow \frac{U}{2} \mathbf{\Gamma}_i$, so that the $\mathbf{\Gamma}_i$ is dimensionless. This leads to the effective electronic Hamiltonian used in the text:

$$H_{el} = \sum_{ij}^{\alpha\beta} \tilde{t}_{ij}^{\alpha\beta} c_{i\alpha}^\dagger c_{j\beta} - \tilde{\mu} \sum_i n_i - \frac{U}{2} \sum_i \mathbf{\Gamma}_i \cdot \mathbf{O}_i$$

Taking the double exchange and superexchange terms also into consideration, one has an effective Hamiltonian for the orbital and spin variables:

$$H_{eff}\{\mathbf{S}_i, \mathbf{\Gamma}_i\} = -\frac{1}{\beta} \log \text{Tr} e^{-\beta H_{el}} + \frac{U}{4} \sum_i \mathbf{\Gamma}_i^2 + J_{AF} \sum_{\langle ij \rangle} \mathbf{S}_i \cdot \mathbf{S}_j$$

where the effect of double exchange is included in the hopping term. The localized spin and orbital moment configurations follow the distribution

$$P\{\mathbf{S}_i, \mathbf{\Gamma}_i\} \propto \text{Tr}_{cc^\dagger} e^{-\beta H_{eff}}$$

We solve the coupled 'fermion - local moment - orbital moment' problem by a Monte-Carlo sampling of the functional $H_{eff}\{\mathbf{S}_i, \mathbf{\Gamma}_i\}$ and obtain equilibrium configurations $\{\mathbf{S}_i, \mathbf{\Gamma}_i\}$. Physical observables are averaged over equilibrium Monte Carlo configurations.

Optical and d.c conductivity

The optical conductivity for the molybdates is calculated by using the Kubo formula [5] as follows,

$$\sigma^{xx}(\omega) = \frac{\sigma_0}{N} \sum_{n, n'} \frac{f(\epsilon_n) - f(\epsilon_{n'})}{\epsilon_{n'} - \epsilon_n} |\langle n | J_x | n' \rangle|^2 \delta(\omega - (\epsilon_{n'} - \epsilon_n))$$

Where J_x is the current operator, given by,

$$J_x = -i \sum_{i,\alpha\beta} \left[(\tilde{t}_{i,i+\hat{x}}^{\alpha\beta} c_{i,\alpha}^\dagger c_{i+\hat{x},\beta} - \text{hc}) \right]$$

$f(\epsilon_n)$ is the Fermi function, ϵ_n and $|n\rangle$ are the single particle eigenvalues and eigenstates of $H_{el}\{\mathbf{S}_i, \mathbf{\Gamma}_i\}$ respectively. The conductivity is in units of $\sigma_0 = \frac{e^2}{\hbar a_0}$, where a_0 is the lattice constant. N is the total number of lattice sites (for a $L \times L \times L$ pyrochlore lattice $N = 4L^3$). Our results are averaged over 50 equilibrium Monte Carlo configurations. The d.c. conductivity is obtained as a low frequency average of the optical conductivity over a window $\sim 0.05t$.

Parameter calibration

In our calculation, $a_0 = a/4$, where a is the fcc lattice constant. For molybdates we have $a \sim 1.0$ nm [6] and thus $\sigma_0 \sim 10^4 (\Omega \text{cm})^{-1}$. For $T \sim 0$, the optical gap Δ is determined by linearly extrapolating the decreasing edge of the optical conductivity spectra in the low energy regime. Fig.5.(a) shows the comparison of experimental gap [7] $\Delta_{expt} = \Delta(r_R)$ and theoretical gap $\Delta_{th} = \Delta(U/t)$ (see figure 5.(b)) at low temperature. We ‘calibrate’ the U/t of our model in terms of r_R based on $\Delta(r_R) \sim \Delta(U/t)$ in the insulating regime (finite optical gap). We try a linear fitting of this data and extrapolate it to lower U/t values, to have an estimate of the U/t in terms of r_R in the metallic regime (zero optical gap). Our calibration (see figure 5.(c)) suggests that for the rare-earth molybdates

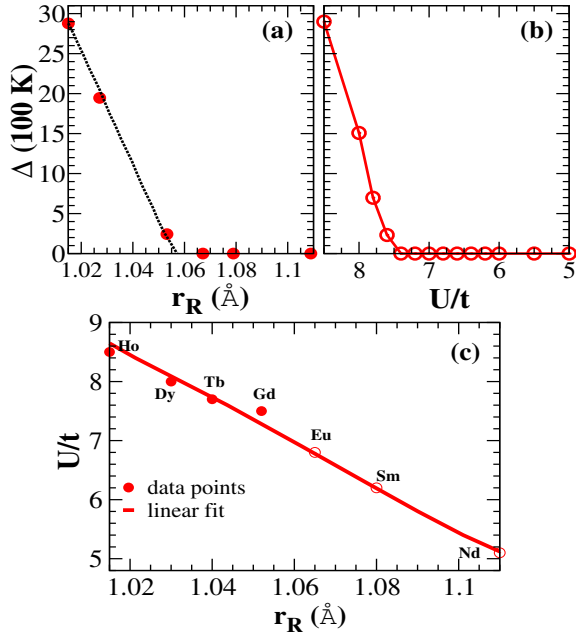


FIG. 5. Optical gap Δ extracted from the low temperature optical conductivity: (a) experiment [7] $\Delta_{expt} = \Delta(r_R)$ and (b) theory $\Delta_{th} = \Delta(U/t)$. (c) $\Delta(r_R) \sim \Delta(U/t)$ gives us the values of U/t appropriate for the rare-earth molybdates.

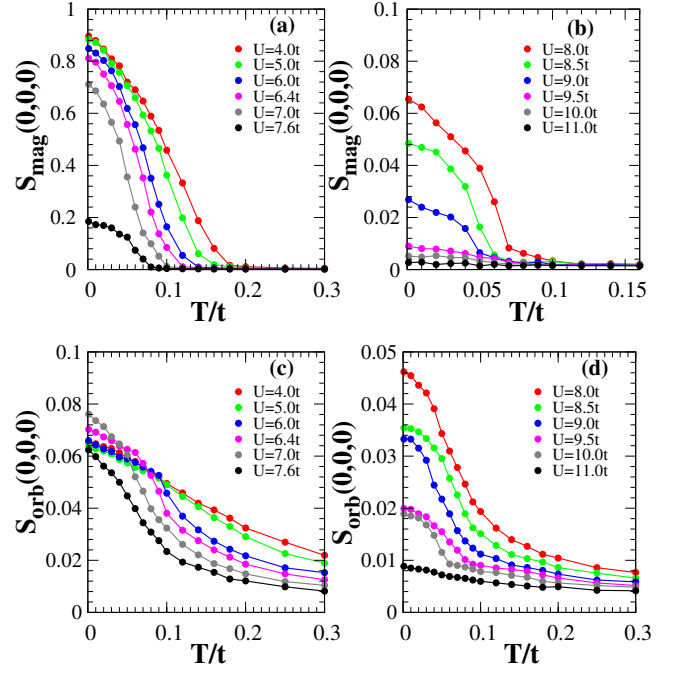


FIG. 6. (a)-(b) show the temperature dependence of magnetic structure factor at $\mathbf{q} = (0, 0, 0)$. We clearly see the rapid growth of ferromagnetic peak below T_c . (c)-(d) show the temperature dependence of orbital structure factor at $\mathbf{q} = (0, 0, 0)$.

the appropriate U/t value varies from $\sim 5 - 9$ as R varies from Nd to Ho.

Structure Factor

We calculate the thermally averaged magnetic structure factor $S_{mag}(\mathbf{q}) = \frac{1}{N^2} \sum_{ij} \langle \mathbf{S}_i \cdot \mathbf{S}_j \rangle e^{i\mathbf{q} \cdot (\mathbf{r}_i - \mathbf{r}_j)}$ and orbital structure factor $S_{orb}(\mathbf{q}) = \frac{1}{N^2} \sum_{ij} \langle \mathbf{\Gamma}_i \cdot \mathbf{\Gamma}_j \rangle e^{i\mathbf{q} \cdot (\mathbf{r}_i - \mathbf{r}_j)}$ at each temperature. These results are averaged over 100 equilibrium Monte Carlo configurations. We use the notation $\mathbf{q} = \frac{2\pi}{L}(n_x, n_y, n_z)$, where the n 's are integers. The onset of rapid growth in the structure factor at some \mathbf{q} , indicates long-range ordering in the system. In Fig.6, we plot the temperature dependence of magnetic and orbital structure factor at $\mathbf{q} = (0, 0, 0)$. We plot the magnetic and orbital structure factors in \mathbf{q} space in Fig.11 and 12 respectively.

Density of States

We calculate the single particle density of states (DOS) $D(\omega) = \frac{1}{N} \langle \sum_n \delta(\omega - \epsilon_n) \rangle$ at each temperature where ϵ_n are the single particle electronic eigenvalues on an equilibrium configuration and $\langle \dots \rangle$ represents averaging over equilibrium configurations. Our DOS results are averaged over 100 equilibrium Monte Carlo configurations.

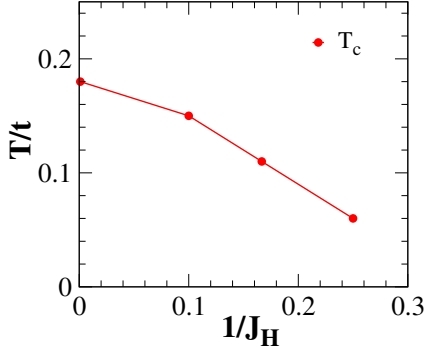


FIG. 7. Variation of the ferromagnetic T_c with Hund's coupling J_H [8]. This result on the single orbital model indicates that the T_c reduces to about half when J_H is lowered to $\sim 5t$ from infinity.

Effect of finite Hund's coupling

To simplify the study of our starting model, we have considered the Hund's coupling (J_H) as infinite. This facilitates to retaining only one species (spin) of electrons in the two orbitals at a site. In reality, however, J_H is finite for all materials. As we decrease J_H from infinite, we observe the lowering of the ferromagnetic T_c . We show the dependence of T_c with J_H in Fig.7.

Variational calculation

We tried a simple variational check on the quality of our Monte Carlo 'ground state'. The $L \times L \times L$ pyrochlore lattice has $N = 4L^3$ sites. We set up trial configurations with ferromagnetic spin and orbital configuration with uniform magnitude $|\Gamma_i| = \Gamma$. Treating Γ as a variational parameter we minimize the energy. The ground state is the configuration with minimum energy. This differs from the real situation where the Γ_i have some amplitude inhomogeneity. We compare the energy and average orbital moment results of the variational calculation with Monte Carlo method (Fig.8). For the Monte Carlo state $\Gamma_{avg} = (1/N) \sum_i \langle |\Gamma_i| \rangle$ where $\langle \dots \rangle$ represents averaging over 100 equilibrium configurations.

We observe that the Monte Carlo and variational results are similar but the Monte Carlo energies are slightly lower.

Computational checks

System size dependence

In order to check the finite size effects on the Monte Carlo results, we have compared our $6 \times 6 \times 6$ lattice (864 sites) calculation with that on a $8 \times 8 \times 8$ lattice (2048 sites). In Fig.9 we compare the ground state magnetization, average orbital moment and the ferromagnetic critical temperature for these

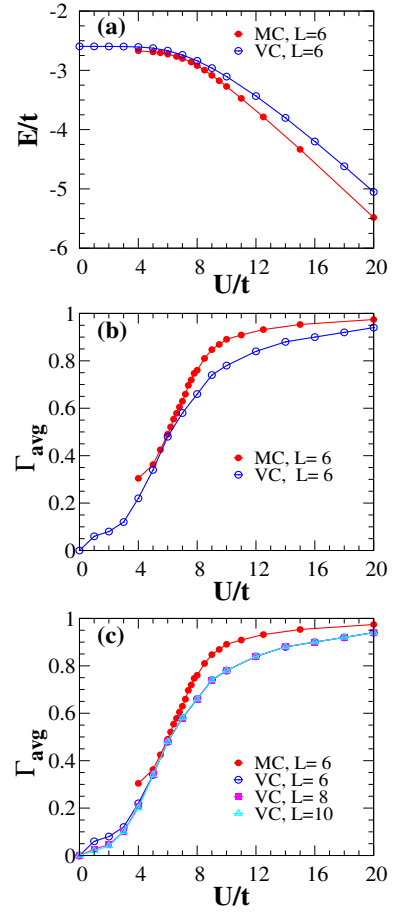


FIG. 8. (a) Energy per site, calculated within variational and Monte-Carlo schemes. (b) Comparison of average orbital moment values computed within Monte-Carlo and variational calculation for same system size. (c) Comparison of average orbital moment values calculated within Monte Carlo and variational calculation with different lattice sizes.

two sizes. The results indicate that by the time $N \sim 1000$ the finite size effect on thermodynamic properties is negligible.

Annealing Time dependence

We compare results obtained for two different Monte Carlo 'annealing time' in Fig.10. We show results on the ground state magnetization, average orbital moment and temperature dependence of the $\mathbf{q} = (0, 0, 0)$ magnetic structure factor for a 2500 MC sweeps/temperature run and a 5000 MC sweeps/temperature run. The temperature discretisation is $0.005t$. The 5000 MCS run takes about 10 days. Our results show that annealing time doesn't alter the results significantly once the run time is $\gtrsim 10^3$ MCS/temperature.

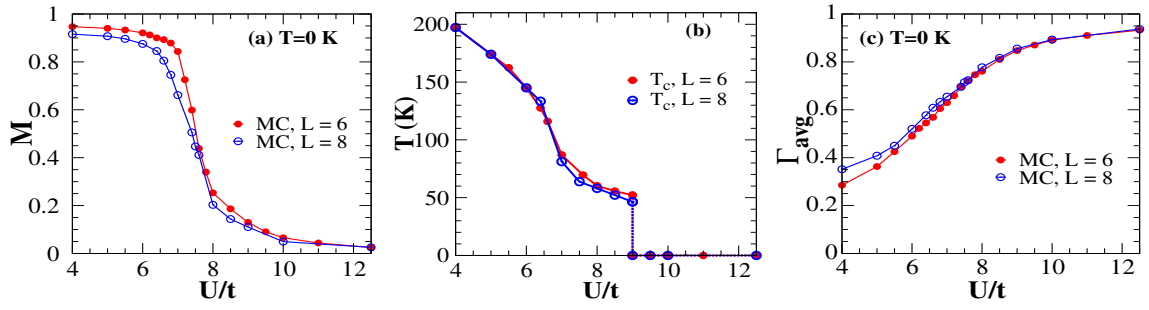


FIG. 9. Comparison of (a) $T = 0$ magnetization, (b) ferromagnetic critical temperature, and (c) average orbital, calculated on $6 \times 6 \times 6$ and $8 \times 8 \times 8$ pyrochlore lattices. The overall system volumes differ by about 3, but the difference in physical properties is negligible.

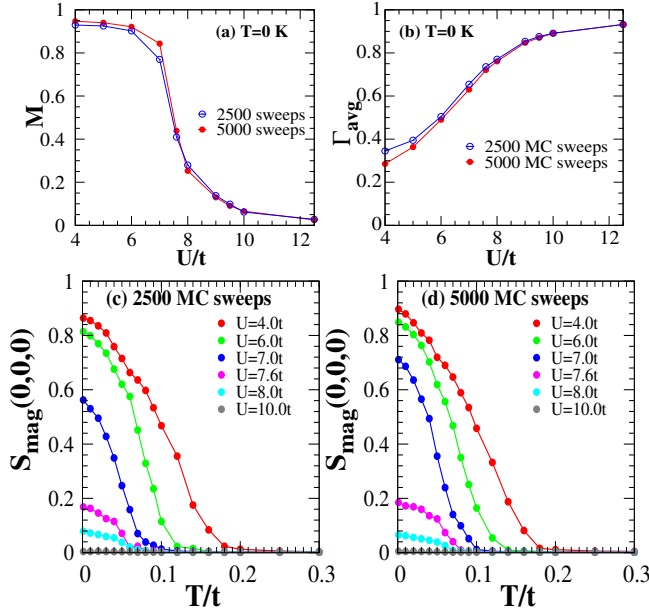


FIG. 10. Annealing time dependence. (a) $T = 0$ magnetization, (b) average orbital moment, and (c)-(d) temperature dependence of $S_{\text{mag}}(\mathbf{q} = (0, 0, 0))$. Runtimes 2500 and 5000 MC sweeps per temperature, with temperature discretisation $\Delta T = 0.005t$. Size $6 \times 6 \times 6$.

-
- [1] Y. Motome and N. Furukawa, J. Phys.: Conf. Ser. **320**, 12060 (2011).
 - [2] J. Hubbard, Phys. Rev. Lett. **3**, 77 (1959).
 - [3] J. Hubbard, Phys. Rev. B **19**, 2626 (1979).
 - [4] H. J. Schulz, Phys. Rev. Lett. **65**, 2462 (1990).
 - [5] P. B. Allen in *Conceptual Foundation of Materials V.2*, edited by Steven G. Louie, Marvin L. Cohen, Elsevier (2006).
 - [6] I. V. Solovyev, Phys. Rev. B **67**, 174406 (2003).
 - [7] I. Kezsmarki, *et al.*, Phys. Rev. B **73**, 125122 (2006).
 - [8] K. Pradhan and P. Majumdar, Europhys. Lett. **85**, 37007 (2009).

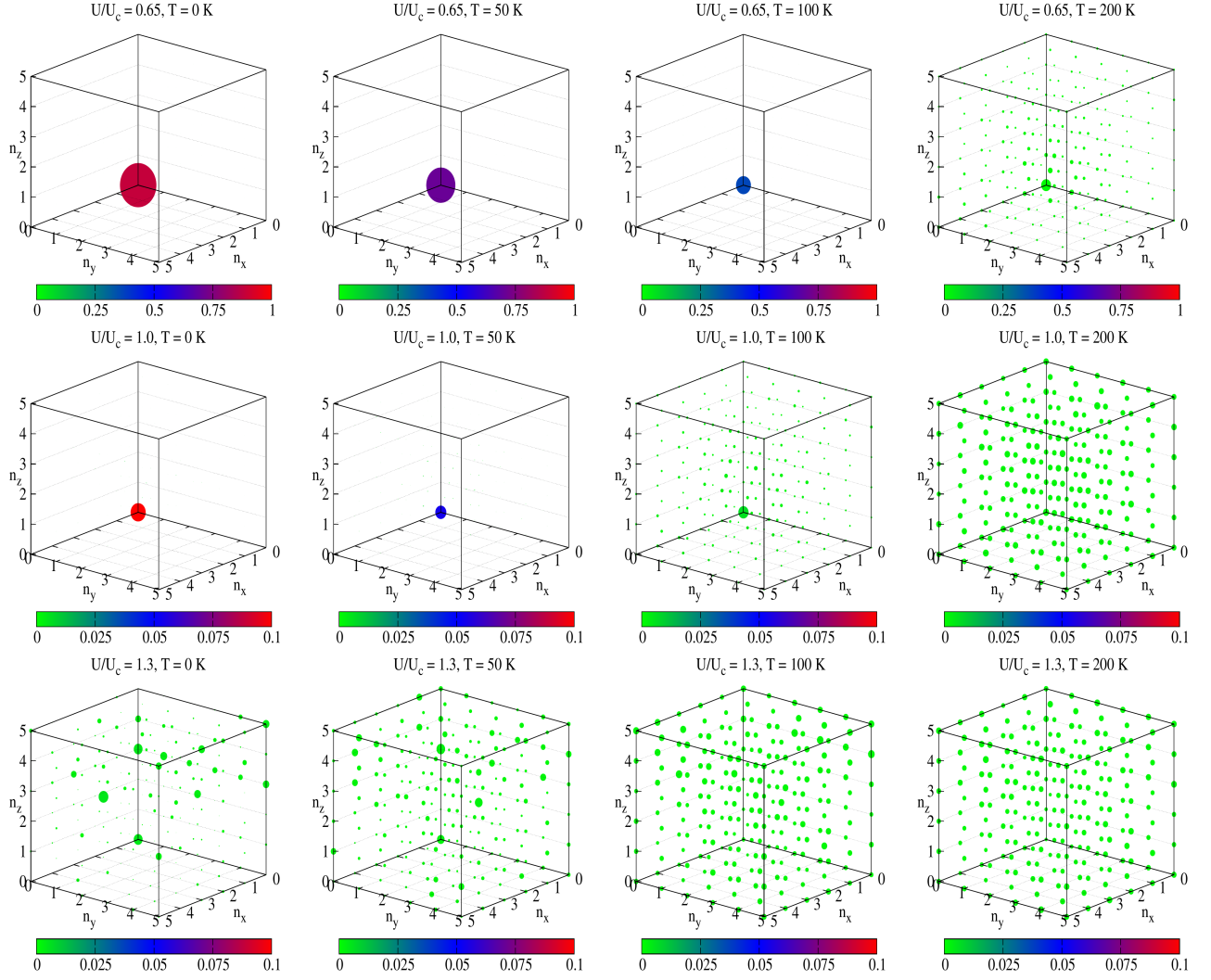


FIG. 11. The full magnetic structure factor $S_{mag}(\mathbf{q})$ for $U = 0.65U_c, U_c, 1.3U_c$ (along column) and $T = 0\text{K}, 50\text{K}, 100\text{K}$ and 200K (along row). We use the notation $\mathbf{q} = \frac{2\pi}{L}(n_x, n_y, n_z)$, where n_i 's are integers and $0 \leq n_i < L$. For the above results, $L = 6$. The size of a dot signifies relative weight at a given \mathbf{q} while its color represents the actual magnitude of $S_{mag}(\mathbf{q})$. For $U = 0.65U_c$ and $T = 0$, $S_{mag}(\mathbf{q})$ has dominant weight $\mathcal{O}(1)$ at $\mathbf{q} = (0, 0, 0)$, indicating ferromagnetic order. With increase in T the weight at $\mathbf{q} = (0, 0, 0)$ reduces gradually and for $T = 200\text{K}$, the weight is distributed among all \mathbf{q} 's - signifying a paramagnet. For $U = U_c$ and $T = 0\text{K}$, $S_{mag}(\mathbf{q})$ still has dominant weight at $\mathbf{q} = (0, 0, 0)$ but it is one order of magnitude smaller than that at $U = 0.65U_c$. With increase in T this weight reduces quickly and shows paramagnetic behavior at $T \sim 100\text{K}$. For $U = 1.3U_c$, even at $T = 0\text{K}$ $S_{mag}(\mathbf{q})$ has no dominant weight at $\mathbf{q} = (0, 0, 0)$. The pattern indicates a spin disordered but correlated magnetic state. With increase in T one obtains an essentially uncorrelated paramagnetic state.

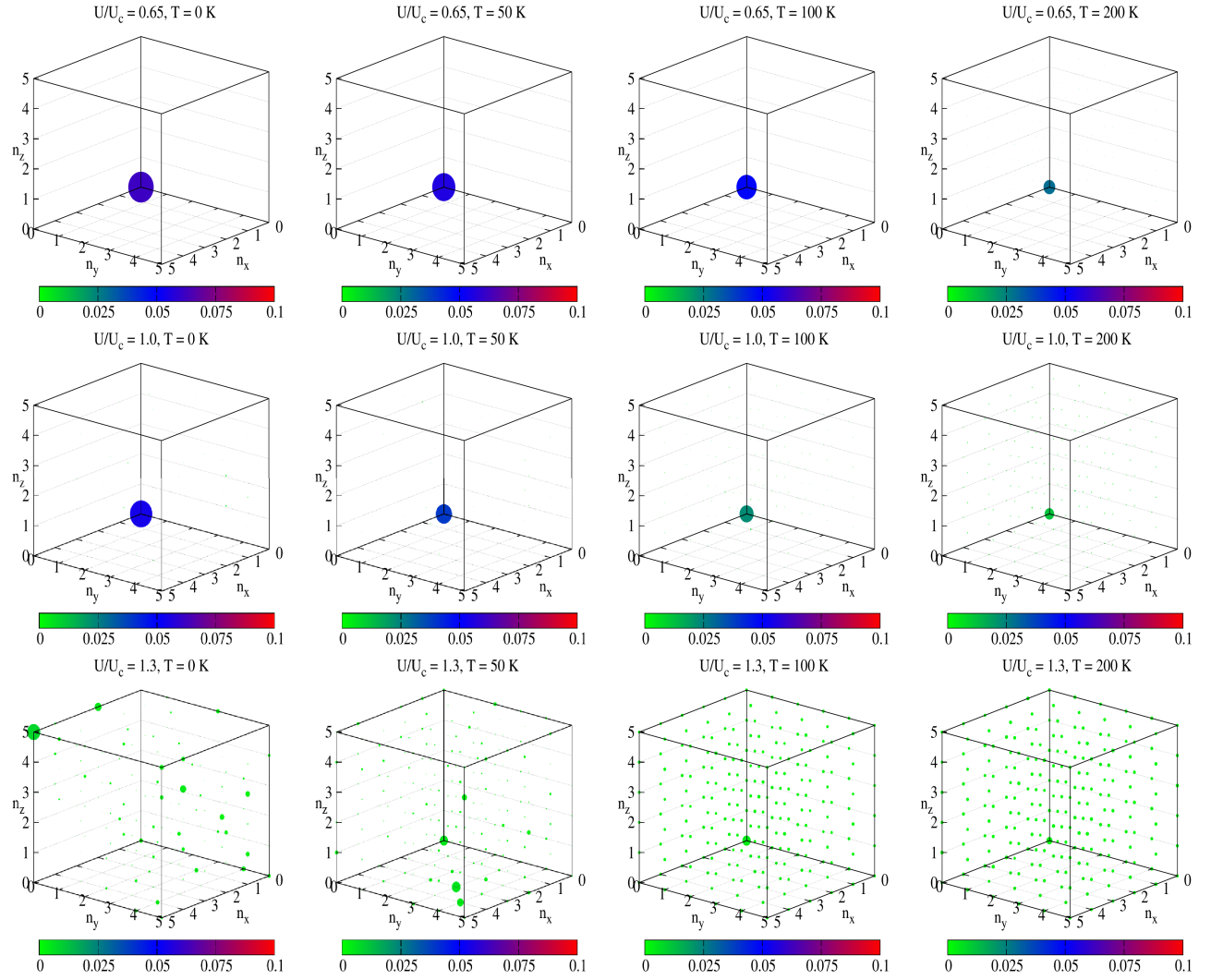


FIG. 12. The full orbital structure factor $S_{orb}(\mathbf{q})$ for $U = 0.65U_c, U_c, 1.3U_c$ (along column) and $T = 0K, 50K, 100K$ and $200K$ (along row). We use the same convention as described in the previous figure. For $U = 0.65U_c$ and $T = 0K$ $S_{orb}(\mathbf{q})$ has weight $\mathcal{O}(0.1)$ at $\mathbf{q} = (0, 0, 0)$, indicating a weak ferro-orbital ordering. With increase in T the weight at $\mathbf{q} = (0, 0, 0)$ reduces gradually. For $U = U_c$ and $T = 0K$ the dominant weight is still at $\mathbf{q} = (0, 0, 0)$. However, this weight is lower than that for $U = 0.65U_c$, indicating the reduction of ferro orbital correlations with increased U values. The $\mathbf{q} = (0, 0, 0)$ weight reduces further with increase in T . For $U = 1.3U_c$, at $T = 0K$, $S_{orb}(\mathbf{q})$ has no dominant weight at $\mathbf{q} = (0, 0, 0)$, rather the $S_{orb}(\mathbf{q})$ weight is distributed unequally among several \mathbf{q} values. This, we feel, indicates an orbital-liquid state due to short range antiferro orbital coupling on the pyrochlore geometry. With increasing temperature the the $S_{orb}(\mathbf{q})$ weight seems to be distributed homogeneously among all \mathbf{q} values, indicating the system entering into a para-orbital phase.